NUMERICAL STUDY OF A CONE MILL FOR EMULSION PREPARATION: HYDRODYNAMICS AND POPULATION BALANCE MODELLING

Guido Lupieri[1]*, Ioannis Bagkeris[1], Jo J.M. Janssen[2], Adam J. Kowalski[1]

[1]Unilever R&D, Port Sunlight Laboratory, Quarry Road East, Bebington, Wirral CH63 3JW, UK
[2]Unilever Foods Innovation Centre, Bronland 14, 6708WH Wageningen, The Nederlands

The work concerns numerical simulations of a cone mill used for emulsion preparation. Hydrodynamics, power consumption and population balance are investigated for various operating conditions at high phase volume emulsions and for different rheologies. Cone mills are usually simplified as a simple gap between rotor and stator but by increasing the complexity of the geometry till it represents the commercial device identifies a wealth of additional features such as recirculation zones above (which enhance breakage) and below (which allow for coalescence) the rotor-stator gap. Two separate sets of population balance modelling constants are required to capture all the experiment results – even with the most complex geometries. Some suggestions are made for improvements and further studies will consider other rotor-stator devices.

Keywords: cone mill, CFD, hydrodynamics, S-γ population balance model

1. INTRODUCTION

The ability to control the drop size of an emulsion is highly desired in many industrial sectors including foods, lubricants, cream and coatings. In particular, we are interested in predicting the drop size of high phase volume emulsions where the drop size and phase volume control the rheology and stability. More specifically our focus is the preparation of a mayonnaise (Dubbelboer et al. (2014)) which is an oil in water emulsion stabilised by the proteins in egg yolk. The preparation can be quickly sketched as a two-step mixing process followed by the filling and packing of jars. In the first step water, vinegar, oil and egg yolk (and optionally flavourings) are mixed together to form a coarse emulsion. In the second step the drop size is further reduced by a high shear mixer to produce a stable product with desired oil droplet size.

The high shear mixer used by Dubbelboer et al. (2016) is a cone mill and is produced by IKA Process Technology (2020). It comprises a rotating frustum surrounded by a gap (< 1 mm) produced by a close-fitting stator, an inlet chamber receiving the emulsion and a collecting chamber from where the product is delivered. The cone mill rotation speed and the gap size can be varied to allow the control of shear rate to deliver the target oil droplet size. The desired gap size is obtained by moving the rotor up or down along its axis relative to the stator and rotation speed is controlled by an electric motor.

---

* Corresponding author, e-mail: Guido.Lupieri@unilever.com

https://journals.pan.pl/cpe

www.czasopisma.pan.pl   PAN   www.journals.pan.pl

G. Lupieri, I. Bagkeris, J.J.M. Janssen, A.J. Kowalski, Chem. Process Eng., 2021, 42 (4), 295–320

Dubbelboer et al. (2016) sought to correlate the measured drop size with operating conditions (specifically shear rate) and the composition. However, despite extensive evaluation they were unable to obtain a single model that correlated all the data. Their model assumed simple shear in the gap between rotor and stator as the only important hydrodynamic feature. The purpose of our study was to provide a more detailed examination of the hydrodynamics in the gap and the upstream and downstream mixer geometry of the mixer in order to improve the prediction of the drop size.

The modelling of the cone mill is a combination of computational fluid dynamics and population balance modelling (PBM). The hydrodynamic field is represented by momentum and continuity conservation and details the local shear rates. The shear rate is then used by the population balance modelling to predict a drop size (Janssen and Mayer (2016) and Janssen and Hoogland (2014)). Power consumption comes from shear and pressure integration and will depend on gap size, viscosity and inlet mass flow rate (e.g. Rapley et al. (2008)). The hydrodynamic analysis is crucial to detect instabilities occurring in the gap between rotor and stator walls which can make the emulsion preparation hard to control and also to model numerically (Maindarkar et al. (2014)).

Tuning of the PBM can be difficult and often it is limited to a fairly narrow operating space. Dubbelboer et al. (2016) were not able to find a universal set of PBM parameters that covered all the data points and our own initial studies (Lupieri et al. (2019)) were able to only partially reproduce the experimental results. Similarly, Buffo et al. (2019) using open source software were only able to reproduce a few of the results. It was unclear if this was a reflection of the simplified hydrodynamics or the sensitivity to the PBM parameters (Lupieri et al. (2019)). The aim of the present study is therefore to assume the model in Dubbelboer et al. (2016), investigate the CFD, PBM and their coupling to identify a universal set of PBM parameters. It is useful to note that devices for emulsion preparation are frequently designed to perform and produce in predictable conditions: clear gap and nominal shear dependence should be ideally assumed by a factory or pilot plant engineer approaching the production of a good, to establish a priori and control the desired characteristics of a product, for instance the final Sauter mean diameter. This made us accept the simple shear approximation in Dubbelboer et al. (2016) and investigate the effects of geometry instead. Rather than jump straight to the most detailed and hence complex geometry which will require considerable computing power to solve, we start with a very simplified version of the cone mill geometry and then gradually add geometric detail to it. We select the geometries so that we can compare them with literature examples of the hydrodynamics modelling to ensure our CFD methodology is consistent with best practice. Having demonstrated this, we then apply the PBM and evaluate the results through comparison with experimental drop size distributions.

The topic of the numerical modelling of a dispersed system in high shear devices is broad since it can cover bubbles or droplets (as in the current work) or even aggregates as in Bałdyga et al. (2007). In that case, the studied device was a Silverson 150/250 which is frequently adopted in emulsion preparation at pilot scale and is intended to be the target of further investigations of the authors of this work, taking advantage from the results of both the mentioned work and the results here presented. In particular, the work of Bałdyga et al. (2007) has shown how the rotor stator configuration was less efficient than a high-pressure nozzle disintegrator system in the breakage process, which was a delicate topic since, at high rotational speed (above 10,000 rpm) and due to the high suction in the rotor proximity, the Silverson 150/250 could develop undesired cavitation, witnessing high pressure drop effects in conjunction with the shear developed between blades and screens leading to possible difficulties in its management.

Another crucial aspect in the numerical modelling of the dispersed phase through Population Balance is that it can be subjected to both laminar or turbulent regime of the carrying phase as considered in Bałdyga and Podgórska (1998) where a model for the breakage was developed to include turbulence intermittency. In particular, the drop breakage was discussed in the inertial regime and controlled by Weber number. This is a crucial point since in the same high shear mixers it is possible to have inertial and viscous

regimes coexisting and associated to different regions of the device and possibly responding to diverse non dimensional numbers.

The numerical analysis of dispersed systems through Population Balance Modelling (PBM) described in Bałdyga et al. (2018) in its general formulation, consists of a nonlinear-integro-partial-differential equation, solved for instance by using the quadrature method of moments (QMOM) as in Jasińska et al. (2014). Among the possible approaches, the $S - \gamma$ method of moments, as implemented by Lo and Zhang (2009) is adopted here. Due to its standard formulation, in the followings are reported only the details strictly necessary for the discussion. The model consists of two transport equations, one for the particle number density n (zeroth moment, $S = 0$) and one for the interfacial area density (second moment, $S = 2$).

When the phase volume fraction α is also available, the method can deliver the Sauter mean diameter of a dispersed phase as:

$$d_{32} = \frac{6\alpha}{\pi S_2} \tag{1}$$

The general form of the assumed transport equation reads as:

$$\frac{\mathrm{d} S_\gamma}{\mathrm{d} t} = S_{br} + S_{cl} \tag{2}$$

where the balance between droplet breakage and coalescence is expressed in the source term. The coalescence contribution reads as:

$$S_{cl} = \left(2^{\gamma/3} - 2\right) C_r C_p d_{\mathrm{eq}}^\gamma \tag{3}$$

In the current numerical simulations, the dispersed phase is subjected to the viscous regime. Here is reported the corresponding and necessary physics. The collision rate C_r reads as a function of the dispersed phase fraction ϕ_d and the shear rate $\dot{\gamma}$:

$$C_r = K_1 \frac{24 \phi_d^2 \dot{\gamma}}{\pi^2 d_{\mathrm{eq}}^3} \tag{4}$$

the coalescence probability C_p includes coalescence time scale t_{cl} (drainage time) as:

$$C_p = \exp\left(-K_2 t_{cl} \dot{\gamma}\right) \tag{5}$$

In the current model, the Capillary number is defined as:

$$\mathrm{Ca} = \frac{\eta_{em} d_{32} \dot{\gamma}}{2\sigma} \tag{6}$$

including apparent emulsion viscosity (further defined) as the emulsion is dense. Breakage occurs when Capillary number exceeds a critical value. de Bruijn (1989) provided the simple shear correlation of data in Figure 1, adopted in the current investigation that assumes the model in Dubbelboer et al. (2016). Nevertheless, when elongational properties are also included, a smaller critical Capillary number is sufficient for breakage in the same condition of viscosity ratio. To include this, a flow index ζ is locally defined to identify the flow conditions between the two extremes: $\zeta = 0$ for simple shear and $\zeta = 1$ for extensional flow: Figure 1 is completed including the data from Bentley and Leal (1986) relative to flow regimes with elongational effects.

For a given particle distribution function $P(d)$, the breakage source term is defined as:

$$S_{br} = \int_{d_{\max}}^{\infty} nP(d)b(d)\left(p^{1-\gamma/3} - 1\right)\mathrm{d}(d) \tag{7}$$

with $b(d)$ the breakage frequency. In this work, the definition given by Dubbelboer et al. (2016) is assumed:

$$b(d) = \begin{cases} K_3 t_{br}^{-1}, & \text{if } d > d_{\max} \\ 0, & \text{if } d \le d_{\max} \end{cases} \tag{8}$$

www.czasopisma.pan.pl PAN www.journals.pan.pl

G. Lupieri, I. Bagkeris, J.J.M. Janssen, A.J. Kowalski, Chem. Process Eng., 2021, 42 (4), 295–320
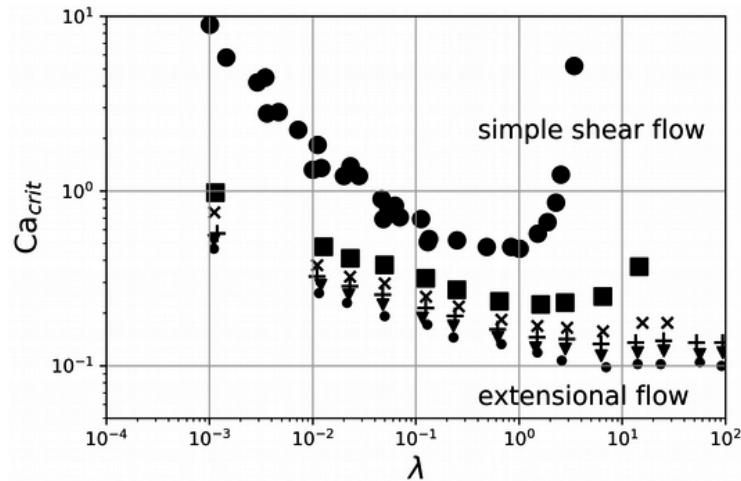
Fig. 1. Capillary number vs viscosity ratio in simple shear and extensional flows. Simple shear flow as solid circle for $\zeta = 0$. Other values of ζ: square (0.2), cross (0.4), plus (0.6), triangle (0.8) and dot (1)

Where $d_{\max}$ is the maximum stable droplet diameter, t_{br} is the breakage time which is estimated from dimensional analysis in the form:

$$t_{br} = \frac{C\eta_{em}d_{32}\lambda^{0.3}}{2\sigma} \tag{9}$$

where $C \cong 60$ has been determined by the experiments of Wieringa et al. (1996). Similar formulations, as for instance in Lo and Zhang (2009), include a polynomial function of viscosity ratio instead of the fitting $\lambda^{0.3}$.

The number of fragments that originated from the breakage reads as:

$$p = 2 + \left(\frac{Ca}{Ca_{crit}}\right)^3 \tag{10}$$

Experimentally derived and assumed in the model of Dubbelboer et al. (2016), the number of fragments is a function of the viscosity ratio, mother droplet size and flow conditions, scaling with $(Ca/Ca_{crit})^3$. The addition of 2 is also present in the mentioned implementation to fit with the daughter droplet size distribution in cases of blunt change between relatively low shear zones (as our inlet) and high shear (as the gap), promoting multiple fragment breakage. The assumption of multiple fragment breakage helps in reaching a maximum steady drop size as soon as the shear rate is sufficient to generate a breakage event, that can occur before the rotor tip is reached.

The maximum steady droplet size $d_{\max}$ is calculated as:

$$d_{\max} = K_4 \frac{2\sigma Ca_{crit}}{\eta_{em}\dot{\gamma}} \tag{11}$$

where σ is the surface tension, $\dot{\gamma}$ is the shear rate and K_4 is another model parameter. Ca_{crit} is the critical Capillary number evaluated using the correlation of de Brujin (1989).

The parameters K_1, K_2, K_3 and K_4 are adjustable model parameters not present in the original formulation of the method but here included to empirically compensate (to some extent) for the fact that the reference breakup criteria are based on assumption of a single droplet in a steady flow, which could not be quantitatively valid for all the considered cases.

The document continues exposing the investigated cases, defines the adopted geometries, rheology and operative conditions. Then, validation and results of the analysis are presented in the third parts. Last, the document finishes with a conclusion including perspectives and references.

2. MATERIALS AND METHODS

Three geometries are used in the CFD with increasing complexity. Geometry 1, CG1 in Figure 2a is a simple truncated cone acting as a rotor surrounded by a close-fitting stator to produce a narrow gap and allows for comparison with the numerical simulations of Li et al. (2014), Buffo et al. (2019) and the experiments of Noui-Mehidi et al. (2005). Li et al. (2014) has an inner rotating cone and no flow through the mixer, aspect ratio $\Gamma = H/d = 12.5$, radius ratio $\varepsilon = R_1/R_2 = 0.8$, cone inclination angle = 82 deg and (rotational) Reynolds number $\mathrm{Re}_r = \dfrac{dR_1\omega}{\nu}$. The experimental work of Noui-Mehidi et al. (2005) uses a truncated cone with a maximum $\mathrm{Re}_r = 730$ after a gradual increase of the rotational speed to produce a pattern of rotating vortices.
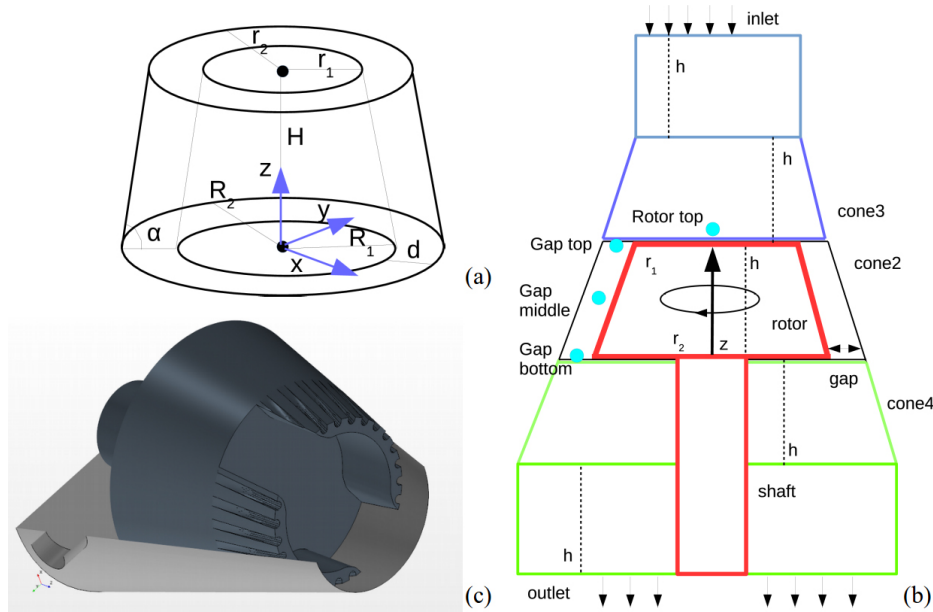
Fig. 2. Topology of all geometries: CG1 on (a), CG2 on (b) and CG3 on (c) with relevant quantities and probe locations

Geometry 2 (CG2) adds a shaft and extrusions of the upper and lower chambers as in Figure 2b and Table 1. Reference for the problem is in Dubbelboer et al. (2014) and Dubbelboer (2016).

Table 1. Relevant quantities of CG2

Object	r_1 [mm]	r_2 [mm]	h [mm]
rotor	23.400	30.000	25.000
gap = 0.624 [mm]			
cone2	24.024	30.624	25.000
cone3	17.424	24.024	25.000
cone4	30.624	37.244	25.000
gap = 0.208 [mm]			
cone2	23.608	30.208	25.000
cone3	17.008	23.608	25.000
cone4	30.208	36.808	25.000

www.czasopisma.pan.pl   PAN   www.journals.pan.pl

G. Lupieri, I. Bagkeris, J.J.M. Janssen, A.J. Kowalski, Chem. Process Eng., 2021, 42 (4), 295–320

Geometry 3 (CG3) of Figure 2c reproduces the features of a complex cone mill by including two grooved blades at the top of rotor in Geometry 2 and the exit pipe is in the side of the outlet chamber as in IKA (2020).

The fluid and drop size properties are taken from Dubbelboer et al. (2016) and are reproduced in Table 2. The name of every test case from M1S1 to M3S5 will be uniquely defined by composing the case labels in Table 2.

Table 2. Simulations executed with reference case label: continuous phase and oil weight fraction (% w/w), initial oil droplet size and parameters assumed for the corresponding rheology curves, flow rate, rotor speed, tip velocity, gap size and corresponding shear rate and residence time

M-label	ϕ continuous	ϕ oil	d_{32} [μm]	$\eta_{r,\infty}$	K	m
M1	0.35	0.65	37.126	1.0	273	0.49
M2	0.30	0.70	35.776	5.9	1800	0.66
M3	0.25	0.75	23.667	9.0	5600	0.70
S-label	flow rate [kg/h]	rotor speed [rpm]	u_{tip} [m/s]	gap [mm]	shear rate [1/s]	t_{res} [s]
S1	31	6039	18.97	0.624	30403	0.31
S2	15	6784	21.31	0.208	102464	0.21
S3	64	3170	9.96	0.624	15959	0.15
S4	15	6039	18.97	0.624	30403	0.64
S5	48	3170	9.96	0.208	47879	0.07

Various models have been proposed for emulsion rheology at high droplet phase fraction, for instance by Bałdyga et al. (2016), but due to its simplicity in implementation and with reference to Dubbelboer et al. (2016), a Sisko model is used here for the relative viscosity of the emulsions:

$$\eta_R = \eta_{r,\infty} + K\,(\dot{\gamma})^{-m} \tag{12}$$

where $\eta_{r,\infty}$, K and m depend upon the oil concentration as in Table 2.

We adopt the effective medium concept in Jansen et al. (2001) where the emulsion viscosity is used as the continuous phase viscosity in the single droplet correlations of Grace (1982). Maindarkar et al. (2014) use this approach to identify the minimum condition leading to the breakage of an oil droplet in the emulsion.

The emulsion is therefore modelled after Park (2018) as a pseudo-single-phase flow obtained from the two separated phases: the oil phase and the continuous phase which is a "matrix" with the other mayonnaise ingredients.

As a consequence, the two phases will have the same kinematic viscosity but different density: $\rho_m = 997$ kg/m^3 for the matrix and $\rho_o = 917$ kg/m^3 for the oil. Similarly, the inlet mass flow rates of Table 2 will split in proportion to the phase fraction and, after the assumption of Park (2018), the viscosity of the continuous phase is computed as:

$$\frac{\eta_a \eta_R \rho_m}{\phi_m \rho_m + \phi_o \rho_o} \tag{13}$$

while the viscosity of the oil is computed as:

$$\frac{\eta_a \eta_R \rho_o}{\phi_m \rho_m + \phi_o \rho_o} \tag{14}$$

where $\eta_a = 0.01$ [Pa s] is the measured aqueous phase viscosity and $\eta_{em} = \eta_a \eta_R$.

From a numerical view point, multiphase flows can be approached as inter-penetrating continua for which there are resolved transport equations for mass, momentum and energy of each phase. Pressure will be in common for all the phases and when no dependence from temperature is assumed, the energy balance is not considered. The numerical method here adopted consists of resolving the hydrodynamics of the problem with a Segregated Finite Volume Navier-Stokes solver and considering a Population Balance Model (PBM) for the dispersed phase. A transport equation for the volume fraction completes the method. Due to the high viscosity, the regime does not require a model for turbulence: the Reynolds number calculated as in Dubbelboer et al. (2016) hardly reaches 200.

The numerical method includes the specification of boundary conditions. With reference to geometry CG1, no-slip on all the fixed surfaces while the inner rotor moves with prescribed rotational speed.

The section completes with the boundary conditions adopted for geometries CG2 and CG3: fixed mass flow rate at the inlet, zero gradient at the outlet (momentum conservation), fixed angular velocity at the rotor and shaft, no slip at the external walls. In absence of a fixed pressure value at the outlet boundary condition and consistently with the adopted solvers, a reference value for pressure is specified in a single cell within the computing domain.

3. RESULTS AND DISCUSSION

This section includes three parts. The first part concerns the study of the hydrodynamics. Geometry 1 of Figure 2a is approached first: validation of results is done against other numerical simulations and experiments. Subsequently the geometry is extended including upper and lower chambers (CG2) and the cases in Table 2 are assumed.

The second part consists of an extensive study of Population Balance Modelling for CG2. The last part extends method and Population Balance Model tuning to CG3.

3.1. Part I

3.1.1. Grid generation and independence

A grid independence study is conducted for the assumed geometries using case M2S1 as a test and examining the following physical properties: pressure, shear rate, relative viscosity along the centre of the gap from bottom to top, vertical velocity component in the radial direction at half gap. Figure 3 reports the results of the study with an increasing grid resolution and includes the results of Buffo et al. (2019), indicated as VIMMP. Quantities are made non dimensional with atmospheric pressure (p_{Ref}), tip speed (u_{Tip}) and nominal shear rate ($\dot{\gamma}_{\text{ref}}$) as in Table 2. The final grid adopted for Geometry 2 is sketched in Figure 4 and comprised 180 nodes along the tangential direction (every 2 degrees) and 30×80 in the radial and axial directions of the rotor.

www.czasopisma.pan.pl   PAN   www.journals.pan.pl

G. Lupieri, I. Bagkeris, J.J.M. Janssen, A.J. Kowalski, Chem. Process Eng., 2021, 42 (4), 295–320
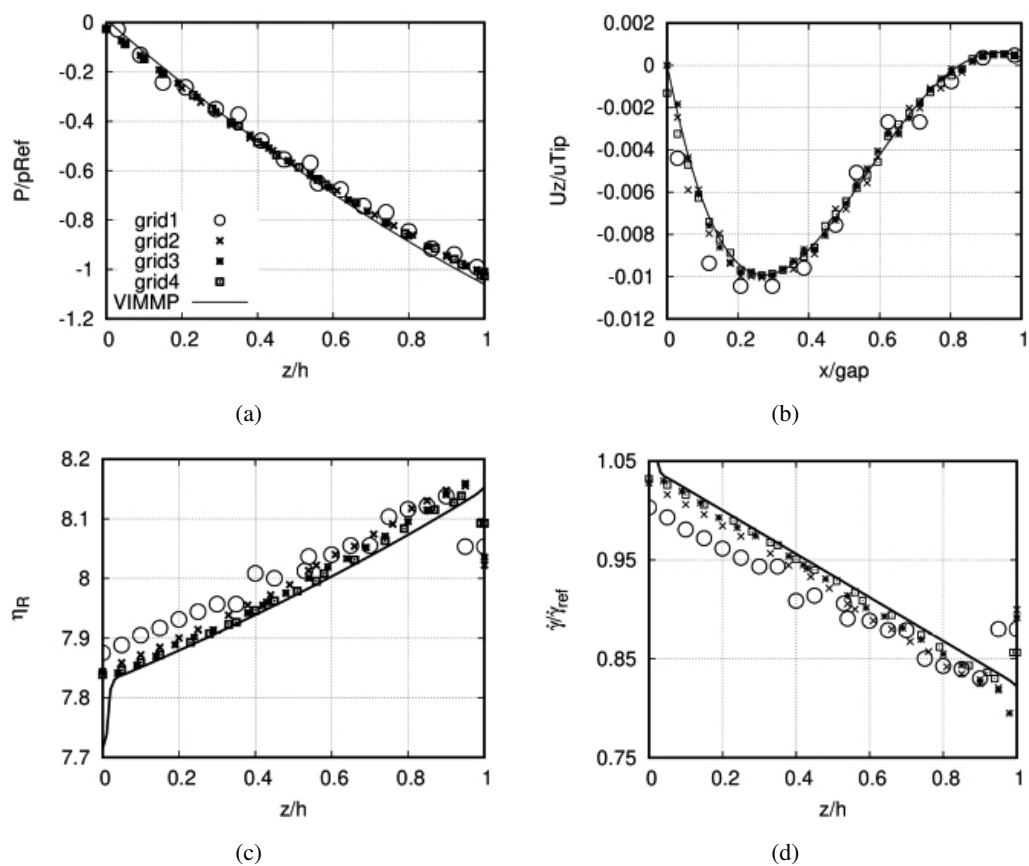
(a)

(b)

(c)

(d)

Fig. 3. Grid independence study: pressure, vertical component of velocity, relative viscosity
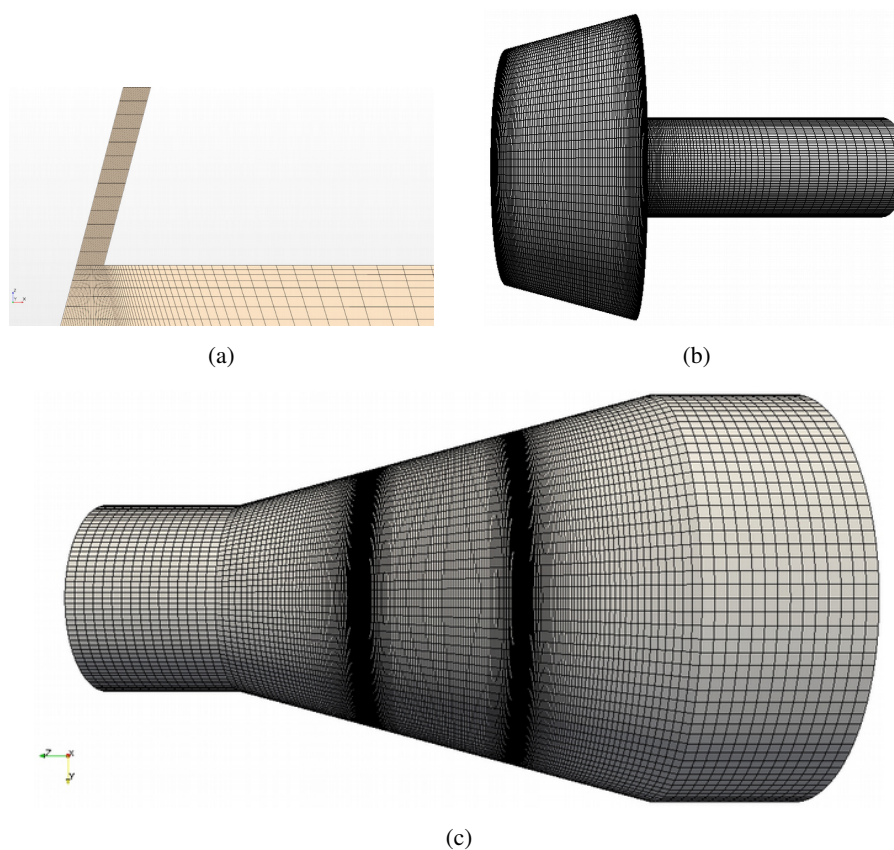and shear rate on (a), (b), (c) and (d) respectively

(a)

(b)

(c)

Fig. 4. Sketches of the computing mesh of Geometry 2: outer gap proximity on (a), rotor on (b)
and a general view on (c)

3.1.2. CFD validation and verification

Geometry 1 reproduces case CG1 in Li et al. (2014). Instabilities are observed at Re = 192.5 (Figure 5a, case vv4 of Table 3): the number of rotating structures corresponds to Li et al. (2014) with the pressure drop at the middle of the gap reproducing the oscillations as seen in the literature is reported in Figure 6. Table 3 also reports that, when the boundary conditions are changed by introducing a mass flow rate or equivalently imposing an inlet velocity from the top of the geometry, instabilities are suppressed, and the pressure drop decreases and becomes positive. The cone geometry can act as a centrifugal pump reducing the pressure drop (vv3) but eventually the pressure drop becomes positive (vv1 and vv2) when the natural pumping capability is lower than the imposed flow.

Table 3. Test cases for validation and verification

Case	u [m/s]	ω [rad/s]	Δp [Pa]	instability
CG1	–	6×10^{-2}	-3.46×10^{-3}	yes
vv1	1×10^{-2}	1×10^{-2}	$+6.15 \times 10^{-2}$	no
vv2	7×10^{-3}	6×10^{-2}	$+3.85 \times 10^{-2}$	no
vv3	1×10^{-3}	6×10^{-2}	-1.05×10^{-3}	no
vv4	1×10^{-4}	6×10^{-2}	-3.24×10^{-3}	yes
vv5	1×10^{-4}	3×10^{-2}	-5.32×10^{-4}	onset

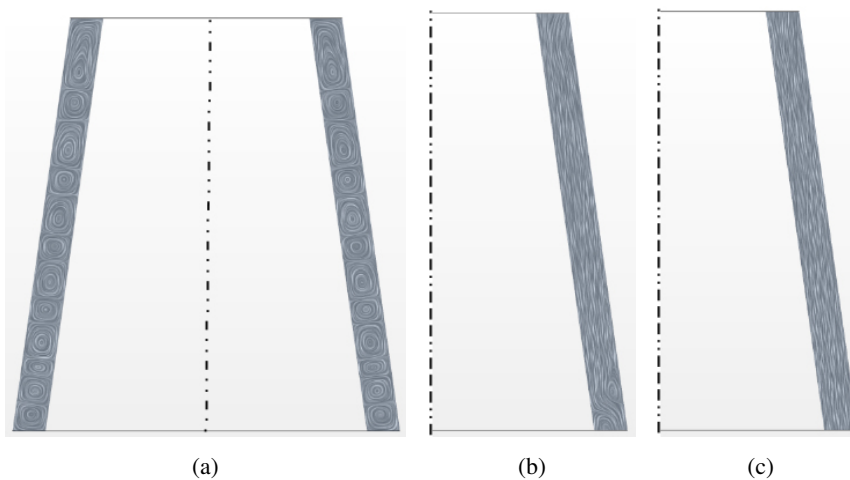(a)   (b)   (c)

Fig. 5. Line integral convolution of velocity field in case CG1: fully developed Taylor vortices on (a), instability onset on (b), instability absence on (c)

Geometry 1 also reproduces Noui-Mehidi et al. (2002) in which the frustum is steadily accelerated at a rate $\beta = 1.3$ [rad/s^2] with a final Re = 730. This time the device has a larger radius at the top than at the bottom and again there is no axial flow at inlet. The numerical simulation reproduced again the number of vortices of the experiments (8) and their relative size (smaller at the top of the device). Figure 7a presents an isosurface of the flow field which is similar to Figure 8.3 of Noui-Mehidi et al. (2002) and a line integral convolution of the velocity, on (b) are sketched with its radial and axial components. Together these two cases indicate that the set-up of the CFD is correct and in the next section we move to reproduce the conditions in Dubbelboer et al. (2016).
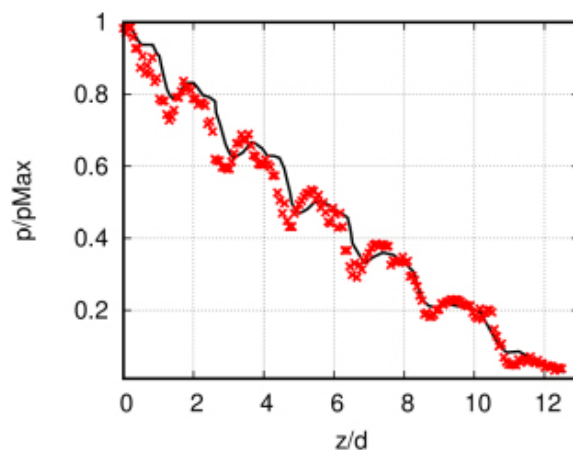
Fig. 6. Pressure along the gap in current investigation (red crosses) vs reference literature (black line)
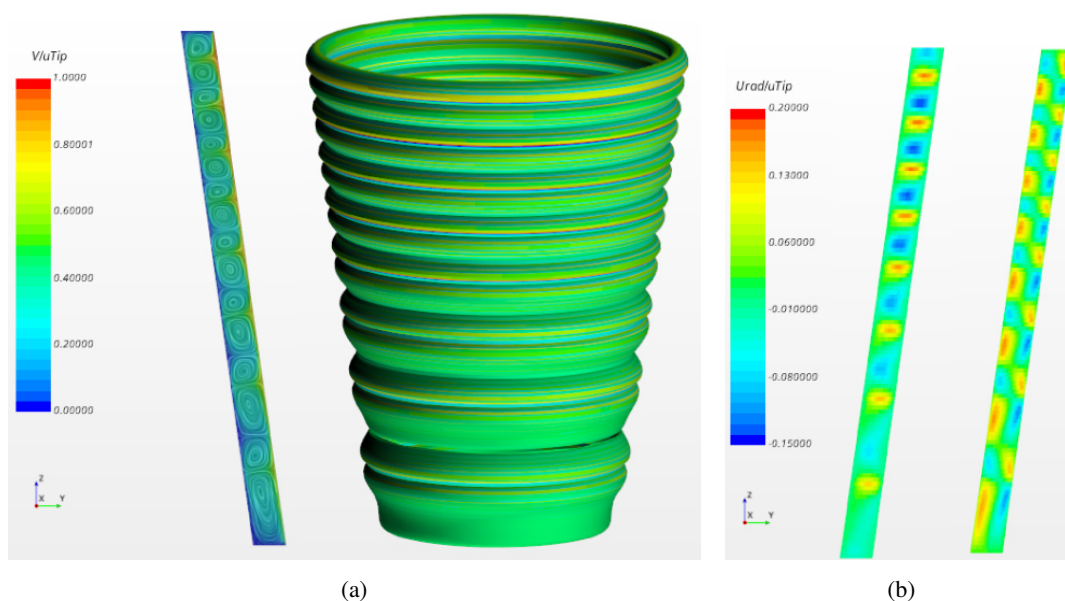

(a)   (b)

Fig. 7. Sketches of velocity fields and flow patterns at $t = 30$ s: line integral convolution and isosurface on (a), radial and axial components respectively on (b)

3.1.3. Hydrodynamics of the cone mill

This section concerns the hydrodynamics of Geometry 2 extending the modelling of Dubbelboer et al. (2016) which only considers the gap since it is the highest shear region. The presence of a chamber at the top of the rotor allows to include its effect at the gap entry and the chamber at its bottom to include any coalescence effects when the fluid leaves the high shear zone. The gap size remains relatively small when compared to rotor radius so the entire domain can be split into well-defined zones. The first one includes the top chamber where the velocity field shows a centrifugal driven recirculation pattern on the top of the rotor which will increase local shear rates that could lead to droplet breakage before the fluid enters the gap. This is sketched in Figure 8a. Figures 8b and 8c show how the gap region, dominated by the rotor speed, can be affected also by secondary recirculation seen in the previous section. Diversely, in the original work, Dubbelboer et al. (2016) assumed simple shear rate in their PBM. Finally, the bottom chamber is a low shear rate region which could allow for some coalescence since in practice egg yolk proteins are large and hence slow to diffuse to stabilise the newly created surface in the gap. The shaft in the bottom chamber plays an important role in the hydrodynamics. Its low tip speed will not cause break

up but it disrupts quasi stagnant flow in the middle of the chamber: this could pollute the delivered droplet size distribution at the outlet. As a consequence, we see that the upper and lower chambers could have a significant impact on PBM.
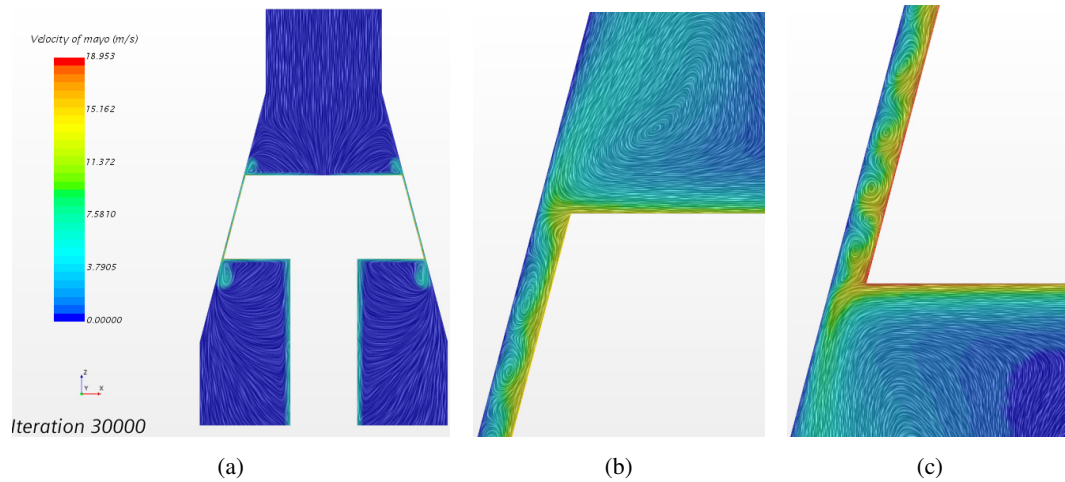

(a)   (b)   (c)

Fig. 8. M1S1: line integral convolution of velocity and instabilities in the gap

Figure 9 shows the pressure field in which the change of sign in pressure drop along the device is evidenced, depending on operative conditions as considered also in the previous section for Geometry 1, reported in Table 3. In the cases with the larger gap, the device is subjected to positive pressure drop (Fig. 9a), negative in the cases of smaller gap (Fig. 9b).

(a)   (b)
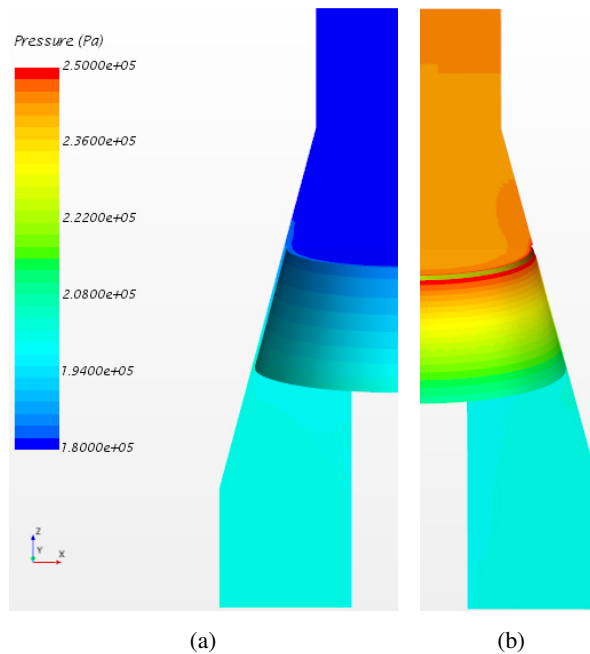
Fig. 9. Examples of pressure fields: case M1S1 on (a) and M2S2 on (b)

Figure 10 presents velocity profiles at the top (Fig. 10a), middle (Fig. 10b) and bottom (Fig. 10c) of the gap. The velocity profile at the gap inlet (a) is a combination of the flow developed in the first chamber with the one determined by the gap rotation: due to the various combinations of imposed mass flow rate, rotational speed and gap size, it would have been difficult to foresee and impose a similar profile in simulations

www.czasopisma.pan.pl   PAN   www.journals.pan.pl

G. Lupieri, I. Bagkeris, J.J.M. Janssen, A.J. Kowalski, Chem. Process Eng., 2021, 42 (4), 295–320

involving a simplified geometry with the gap only as in the previous section. In most cases the axial flow is not parabolic and exhibits evidence of vortices in cases M1S1 and M1S4. On (c) the axial velocity is shown to re-enter fluid in the gap. This effect reduces with the increase of the emulsion viscosity, vanishing in M3.
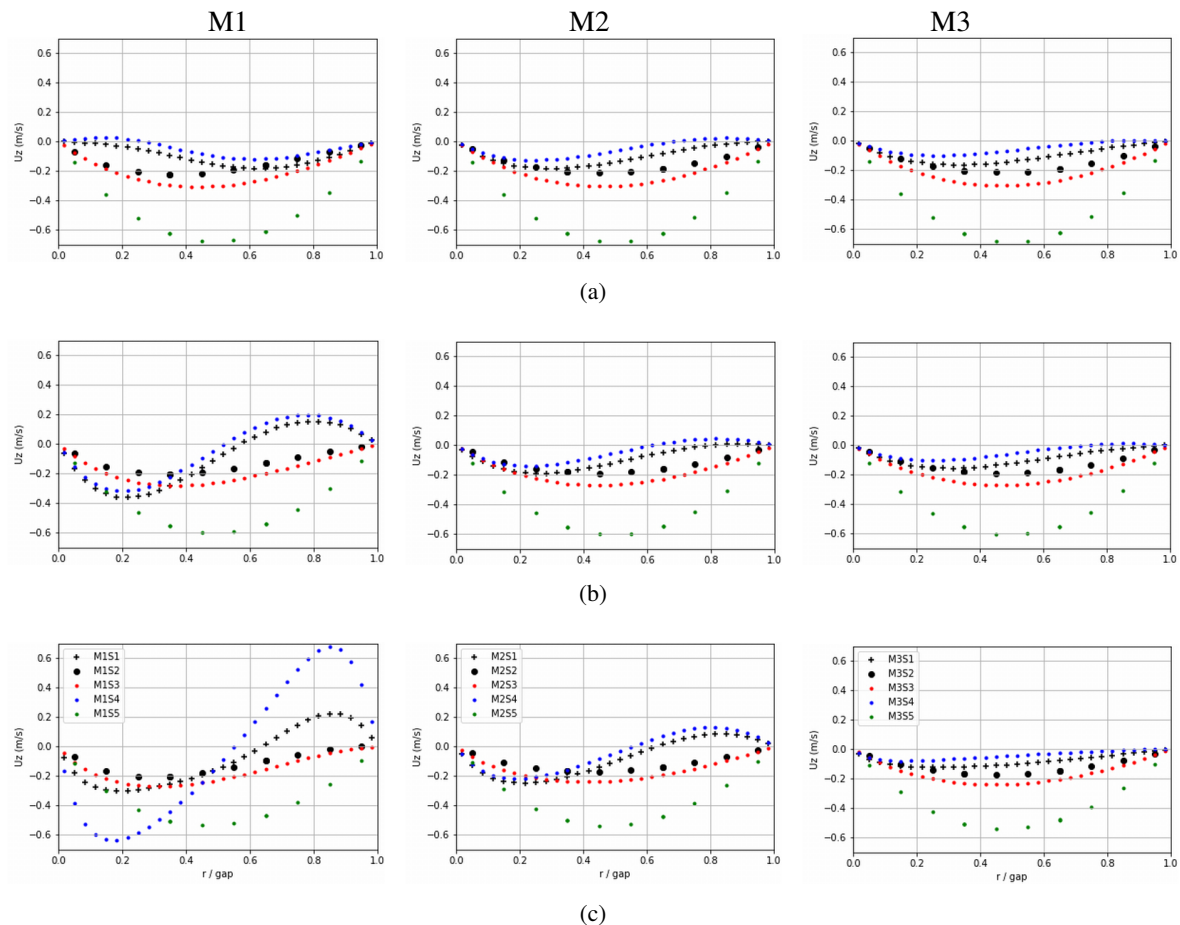

Fig. 10. Mayo M1 to M3 in columns: axial velocity component at the inlet (a), half height (b) and outlet (c) of the gap

The occurrence of instabilities in concentric cylinders subjected to the rotation of the inner one and to an imposed axial pressure gradient has been investigated for instance by Lupetow et al. (1992). Similar cases are often called Taylor Couette Poiseuille (TCP) flows. The axial Reynolds number is defined as $Re_a = w \cdot \text{gap}/\upsilon_{em}$ where the velocity w is assumed from the imposed mass flow rate, υ_{em} is an average value in the gap volume, as in Buffo et al. (2019). The Taylor number $Ta = r_2\omega \cdot \text{gap}/\upsilon_{\text{em}}$ is obtained from the rotational speed. Figure 11 presents a map (Re, Ta) which illustrates the role of flow rate on suppressing the instabilities in the gap and returning to a simple shear rate field. Lupetow et al. (1992) used linear stability calculations to obtain a value for the transition to Taylor vortex flow for the case of zero axial flow of Ta = 108, which is similar to the results of the current computations, reproduced in Figure 11. The map here reported shows how the presence of an axial flow can delay instability occurrence: for example, the pair (Re = 0.5, Ta = 141) still represents a stable condition. The map is enriched with the indication of instability onsets, detected visually as a single vortex at the end of the gap, as sketched in Figure 5b.

Figure 11 completes with a straight line limiting steady and unsteady regimes. In this case, no comparison is directly possible with Figures 4 and 6 of Lupetow et al. (1992) for two reasons: in the first one, a broader range of Reynolds and Taylor numbers was assumed with a consequent coarse resolution in the niche considered in the current investigation and in the second one, Lupetow et al. (1992) evidenced
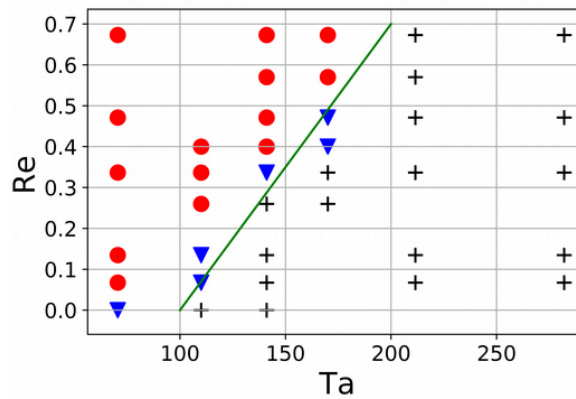
Fig. 11. Taylor vs Reynolds number: + indicates the presence of developed Taylor vortices in the gap, lower triangles indicate instability onset

how geometry of the problem resulted very sensitively to radius ratio but assumed cases are not directly comparable with the current one.

Finally, power draw is considered briefly here: not surprisingly for a highly viscous flow, the majority of the power comes almost entirely from viscous contributes and not from the integral of pressure at the rotor surface. Consequently, in spite of the small size of the device the high phase volume emulsion viscosity pushes the power up to 1KW (Table 4).

Table 4. Geometry 2: power [W] calculated at the rotor from torque and pressure contributes

	S1	S2	S3	S4	S5
M1	119.5	226.1	33.0	121.4	54.6
M2	262.0	662.4	74.6	261.7	150.3
M3	412.6	1023.3	135.7	412.4	253.3

3.2. Part II

Optimisation of PBM model parameters is generally affordable when the flow field is either assumed homogeneous by volume-averaging (so-called 0D lumped PBM) or by introducing a limited degree of flow inhomogeneity (e.g. PDF-based Buffo et al. (2016), 1D Håkansson et al. (2009) and zonal PBM Alopaeus et al. (1999)). However, optimising model parameters in coupled CFD-PBM simulations is computationally intensive. In this exploration, model parameters are varied by several orders of magnitude, to cover a broad range of parameter space, while a limited number of values for each parameter is explored. The aim here is to identify the raw trends of the adopted modelling approach rather than to provide a best fit.

Parameter K_4 relates the critical Capillary number to the maximum steady droplet size, and it is possibly the only parameter that can be experimentally validated in a direct manner. From the effective medium "Grace model" in Jansen et al. (2001), it can be estimated as $K_4 \sim 0$ (1). Some numerical studies Dubbelboer et al. (2016) have adopted this approach, by setting $K_4 = 1$, while in other studies K_4 has been treated as a free parameter (Maindarkar et al. (2014)). Our preliminary simulations showed that, for $K_4 = 1$, predictions for the 65 wt% mayonnaise were insensitive to all operational conditions. A similar trend was observed in Dubbelboer et al. (2016) where the same value was used. By allowing smaller values, the droplet sizes for the 65 wt% mayonnaise became sensitive to operational conditions and improved predictions. In this

www.czasopisma.pan.pl PAN www.journals.pan.pl

G. Lupieri, I. Bagkeris, J.J.M. Janssen, A.J. Kowalski, Chem. Process Eng., 2021, 42 (4), 295–320

study, we explored different values of $K_4 = 0.04, 0.4, 1$ and 4, therefore broadening the investigation space with respect to the range expected from Jansen et al. (2001).

For parameter K_2, previous studies have reported values which span many orders of magnitude in the range of $10^{-3} - 10^{10}$ (Dubbelboer et al. (2014) and Dubbelboer et al. (2016)). We explored three different values $K_2 = 0.01, 1, 100$. In the conceptual framework of a binary collision, as worked out by Chesters et al. (1991), it is depicted that, as the film drainage takes substantially longer than the collision time $(1/\dot{\gamma})$ there should be no coalescence, while coalescence is expected in the opposite limit. This behaviour is exactly captured for $K_2 = 1$, whereas substantially different values of K_2 likely signify break-down of the binary collision assumption in concentrated emulsions.

Parameter K_1 controls the magnitude of coalescence frequency. For each pair of values of K_2 and K_4, the relative effect of coalescence was examined using increasing values of K_1. Finally, for each K_1, K_2 and K_4 triplet, K_3 was estimated from the out flow d_{32} of test case M3S2 and then, the complete set of parameters was used to predict the rest of the test cases. This approach yielded a total number of $3 \times 4 \times 5 = 60$ sets of model parameters, which is a compromise between sufficient exploration of the parameter space and computational cost.

3.2.1. Comparisons with experiment

Sauter mean diameters at the outlet of the device obtained from the simulations are compared with the experiment via the parity plot in Figure 12a. The predictions for test cases S1–S3 are found in reasonable agreement for all three types of mayonnaise. For these test cases, the maximum absolute relative error is 28.92% and the average absolute relative error is 10.25%. Predictions for test cases S4–S5 are weaker as the droplet size is underpredicted. Improved predictions for cases S4–S5 could be obtained but for significantly smaller values of K_1 and K_3 in Figure 12b. In that case, though, agreement for S1–S3 deteriorated and, thus, the overall difference of the simulation results with the experiment was larger than the one obtained using large values of K_1 and K_3. Using these small values of K_1 and K_3 and for S4–S5, the maximum absolute relative error is 10.01% and the average absolute relative error is 6.96%.
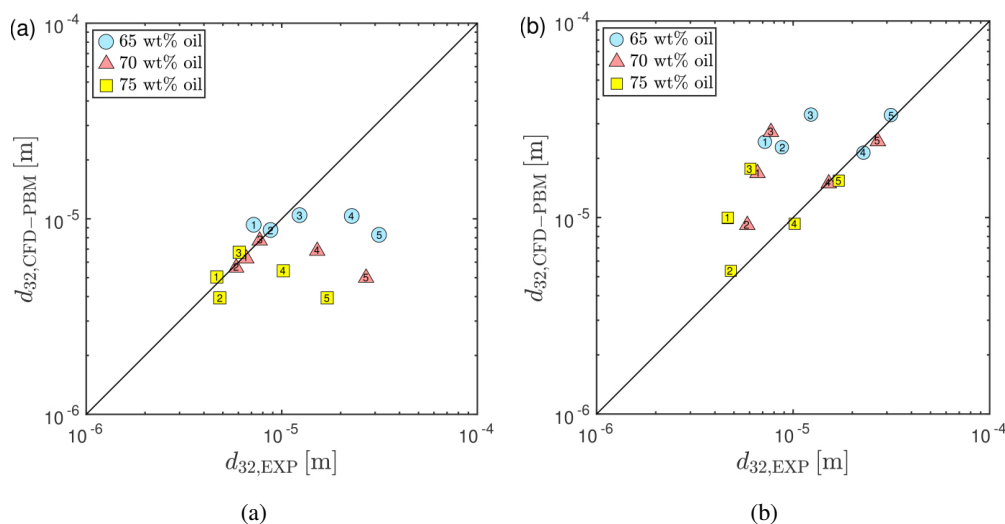

Fig. 12. Parity plot of d_{32} using two sets of model parameters shown in Table 4: Set 1 on (a) and Set 2 on (b). Simulation labels refer to Table 2

From case S1 to case S3, the gap shear rate is varied within its entire range by changing the rotation speed and the gap width. However, the gap residence time is limited to the middle of the range explored (Table 2).

Conversely, in S4–S5 the gap residence time covers the whole while the gap shear rate is limited to middle of the range explored. The numerical simulations revealed that two sets of model parameters are needed to reproduce the experimental results with the desired accuracy. Each set corresponds to the test cases where either the gap shear rate or the gap residence time is varied the most. The values of these two sets of parameters are reported in Table 5. There does not seem to be an obvious explanation of this behaviour which we consider characteristic of the adopted modelling approach, i.e. the combination of the models of breakage frequency, coalescence frequency and daughter size distribution used in this work.

Table 5. Optimised parameter values for the test cases where the gap shear rate is varied and the gap residence time is constant (Set 1) and the gap residence time is varied and the gap shear rate is constant (Set 2)

Set	Test Cases	K_1	K_2	K_3	K_4
1	S1–S3	0.0014	0.01	0.11	0.4
2	S4–S5	0.0004	0.01	0.005	0.4

The value of K_4 which produced best predictions (= 0.4) was found smaller than the one established by several experimental studies ($\approx$ 1) (deBruijn (1989); Grace (1982); Jansen et al. (2001)) but within the same order of magnitude. A likely explanation is the contribution of elongational flow to droplet breakup in colloid mills. The flow field in colloid mills is often idealised as simple shear (Dubbelboer (2016); Maindarkar (2014)), which probably holds in the middle of the gap for sufficiently small Taylor numbers, but it is less likely to hold at the top of the rotor, where the flow accelerates to enter the gap, as well as the gap exit where the flow discharges to the outlet chamber. Experimental studies of elongational flow have identified critical Capillary numbers smaller and of the same order of magnitude than those in simple shear Grace (1982), thereby the value of $K_4 = 0.4$ can be attributed to the combined effect of simple shear and elongational flow on droplet breakup.

In the next section, we analyse the spatial distribution of the droplet sizes obtained using the parameter values in Table 5 for test cases S1–S3.

3.2.2. Droplet dispersion

The velocity field is dominated by the tangential velocity component imposed by the rotor and the shaft; the axial and the radial components remain 1-2 orders of magnitude smaller. Despite their small magnitude, these secondary motions are of great importance because they determine the residence times at the different compartments of the device. Figure 13a shows the d_{32} contour on the vertical plane for the 70 wt% mayonnaise and operating condition S1. Two recirculation regions were observed in the chambers above and below the gap. The secondary flow on this plane is shown in Figure 13b. Half planes are only shown due to symmetry. In the top chamber and above the recirculation zone the droplet size increased near the wall of the inlet chamber due to coalescence. Coalescence is favoured near the wall because of finite shear rates which are small enough so as not to promote breakage. An increase of d_{32} in this region was observed in all the test cases examined. Note that the maximum contour level in Figure 13a has been adjusted to 40 µm to facilitate visualisation of d_{32}. For this case, $d_{32,\text{max}} = 83.2$ µm observed at the location where the flow detaches from the wall of the inlet chamber. The largest $d_{32,\text{max}}$ among all test cases was 152.9 µm, meaning that the predicted droplet sizes remained within physical bounds. The recirculation region is due to the drag on the rotating top of the rotor and centrifugal forces initiating the flow. The high local shear rates cause droplet breakup. At the gap entrance it splits into two streams: one entering the gap and one directed towards the recirculation region.

Breakage frequency shown in Figure 14a suggests that breakage occurs inside the gap, in the boundary layers at the top and the bottom of the rotor, in a small part of the recirculation regions and to a limited
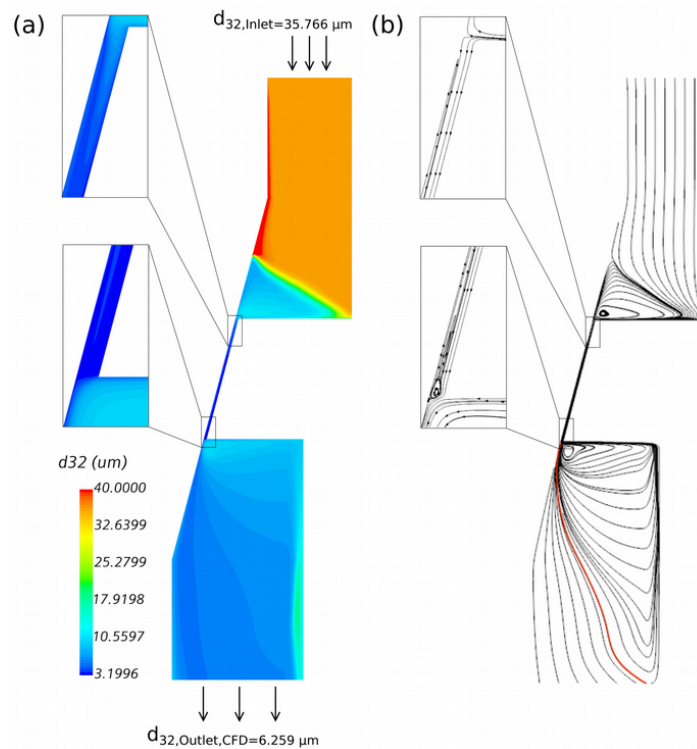
www.czasopisma.pan.pl   PAN   www.journals.pan.pl

G. Lupieri, I. Bagkeris, J.J.M. Janssen, A.J. Kowalski, Chem. Process Eng., 2021, 42 (4), 295–320

Fig. 13. (a) Contour of d_{32} and (b) streamlines for test case M2S1; $d_{32,\text{EXP}} = 6.587$ μm

extent close to the shaft. The number of fragments (Equation 10), shown in Figure 14b peaks at the entrance of the gap, where large droplets encounter large shear. Consequently, the largest change in droplet size is observed in the vicinity of the entry into the gap rather than in the middle region where the flow is expected to be closer to simple shear; this observation is consistent with the earlier explanation that the low value of $K_4 < 1$ is likely to be a contribution of elongational and shear flow to droplet breakup. On the other hand, coalescence is predicted in a much wider part of the domain. Coalescence frequency $C = C_r \cdot C_p$
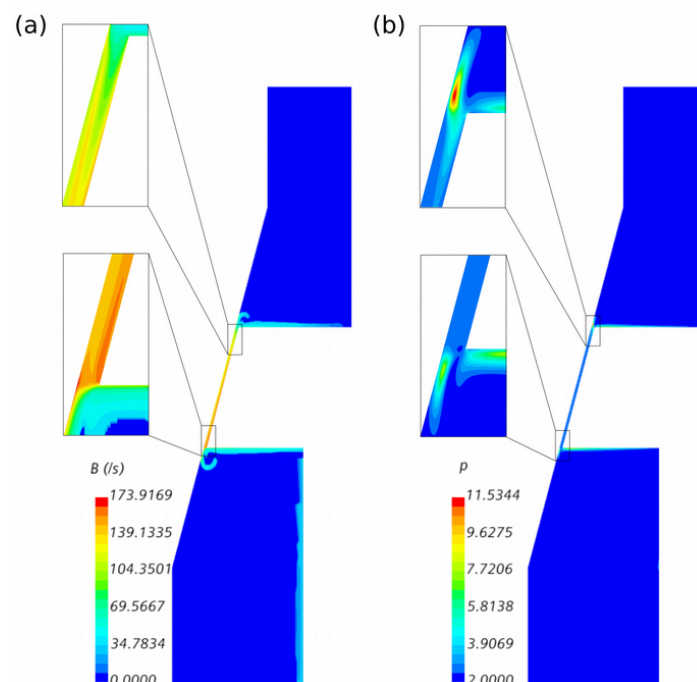
Fig. 14. Contours of (a) breakage frequency and (b) number of fragments for test case M2S1

(Equations 4 and 5) is shown in Figure 15; it is maximum in the gap and of considerable magnitude in the recirculation region of the inlet chamber and the entire outlet chamber.
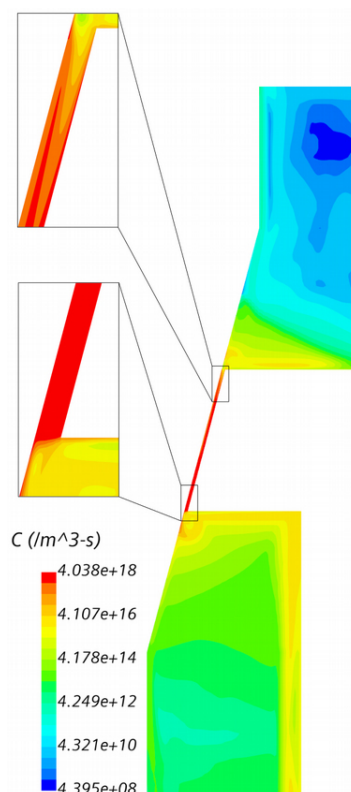
Fig. 15. Contour of coalescence frequency for test case M2S1

Table 6 includes the predicted d_{32} for M2S1 at several locations of the domain; probe locations are visualised in Figure 2b. At the entrance of the gap, $d_{32} = 8$ µm which means that substantial breakage is predicted upstream since d_{32} at the inlet = 36 µm. Drop size reduces continuously along the gap towards its smallest value in the domain (3.6 µm) at the gap walls near the bottom. The reduction rate is larger closer to the top of the gap than closer to the bottom (see zoom in Figure 13a, a Taylor vortex is observed near the gap exit (see zoom in Figure 13b).

Table 6. d_{32} at the locations sketched in Figure 2b for indicated emulsion and operational conditions. The value of d_{32} is uniform at the inlet and surface average at the outlet

Location	d_{32} [µm]				
	M2S1	M1S1	M3S1	M2S2	M2S3
Inlet	35.766	37.126	23.667	35.766	35.766
Rotor Top	18.151	28.781	11.538	12.003	21.932
Gap Top	8.041	11.304	6.658	5.117	20.196
Gap Middle	3.694	5.158	3.448	1.667	7.079
Gap Bottom	3.609	4.914	3.272	1.603	5.151
Outlet	6.259	9.293	5.041	5.624	7.728
Outlet (EXP)	6.587	7.206	4.647	5.844	7.713

25

www.czasopisma.pan.pl   PAN   www.journals.pan.pl

G. Lupieri, I. Bagkeris, J.J.M. Janssen, A.J. Kowalski, Chem. Process Eng., 2021, 42 (4), 295–320

Figure 13a further shows an increase in d_{32} from the gap exit to the outlet of the domain. Droplets passing through the recirculation region in the outlet chamber coalesce due to finite shear rates close to the shaft and the rotor bottom surface. Physically this may in part also be due to the slow diffusion of the egg yolk emulsifier to the newly created surfaces though this is not explicitly incorporated in the PBM equations. These droplets are driven back into the shear layer which develops from the rotor bottom edge, and they are dragged downstream by the stream of freshly broken droplets exiting the gap. The volume of the recirculation region in the outlet chamber is expected to affect d_{32} at the outlet, since, for a larger volume of this recirculation region, more droplets will be subject to conditions which promote coalescence. In Figure 13a, the size of recirculation region in the outlet chamber is indicated via a red streamline, which is the streamline passing through the location at the outlet where the flow reverses. Identifying the size of the recirculating region in the outlet chamber will be useful in the following sections where we compare different test cases. At the same time, a non-recirculating region, relatively smaller in size is present and represents the alternative and preferred way by which droplets can exit more quickly.

3.2.3. Droplet dispersions for different wt% emulsions and same operational conditions

Figures 16 and 17 show contours of d_{32} for the 65 wt% and the 75 wt% emulsion respectively, and S1 operational conditions. Values of d_{32} at several locations are reported in Table 6. In the inlet chamber, the effect of increasing wt%, i.e. of increasing viscosity, is to: (i) decrease the size of the recirculation region, (ii) decrease d_{32} at the centre of the rotor top surface and (iii) decrease the d_{32} at the entrance of the gap. The larger viscosity of the higher phase volume emulsions increases the stresses which in turn enhances breakage in the boundary layer on the rotor top surface and thereby reduces the drop size. The reduction of d_{32} inside the gap is also significantly different; for the 75 wt% emulsion, the smallest d_{32} is much closer to the entrance than for the 65 wt% emulsion. This may be because of the lower stresses (see above) but also we see Taylor vortices will tend to reduce the local shear rates so the breakup is not
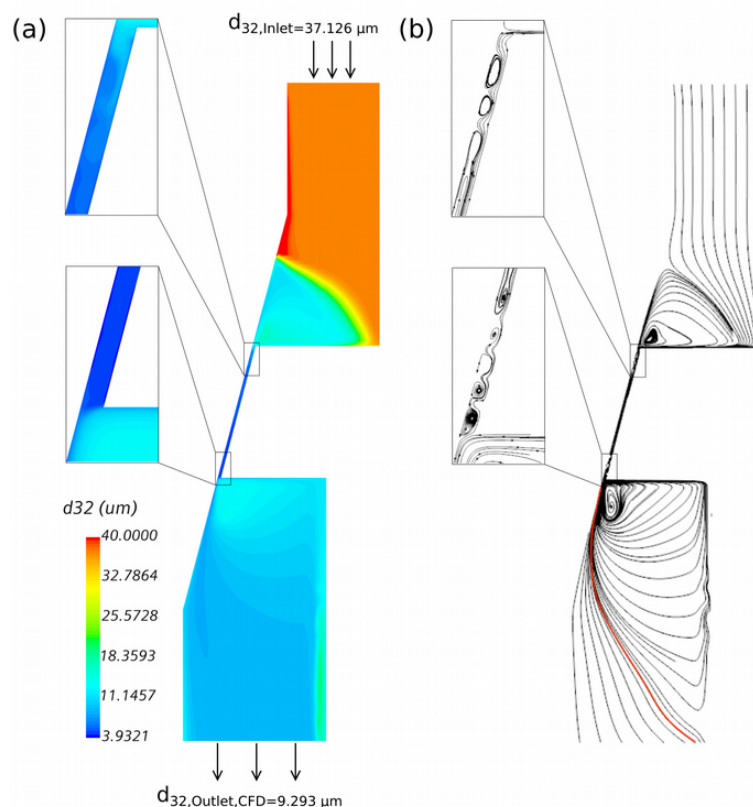

Fig. 16. (a) Contour of d_{32} and (b) streamlines for test case M1S1; $d_{32,\text{EXP}} = 7.206$ μm

as efficient. In the outlet chamber, the increase of d_{32} from the gap exit to the outlet of the domain for the 65 wt% emulsion is larger than the one for the 75 wt% emulsion. This appears to be related to the size and shape of the recirculation region which acts as a source of coalescence. The larger viscosity of the 75 wt% emulsion produces a smaller recirculation zone which will reduce the residence time in the bottom chamber for coalescence to occur. In addition, there is a thicker higher shear layer on the underside of the rotor (see Figure 17b) which will increase the shear rates promoting breakup compared to the respective shear layer of the 65 wt% emulsion (see Figure 16b).
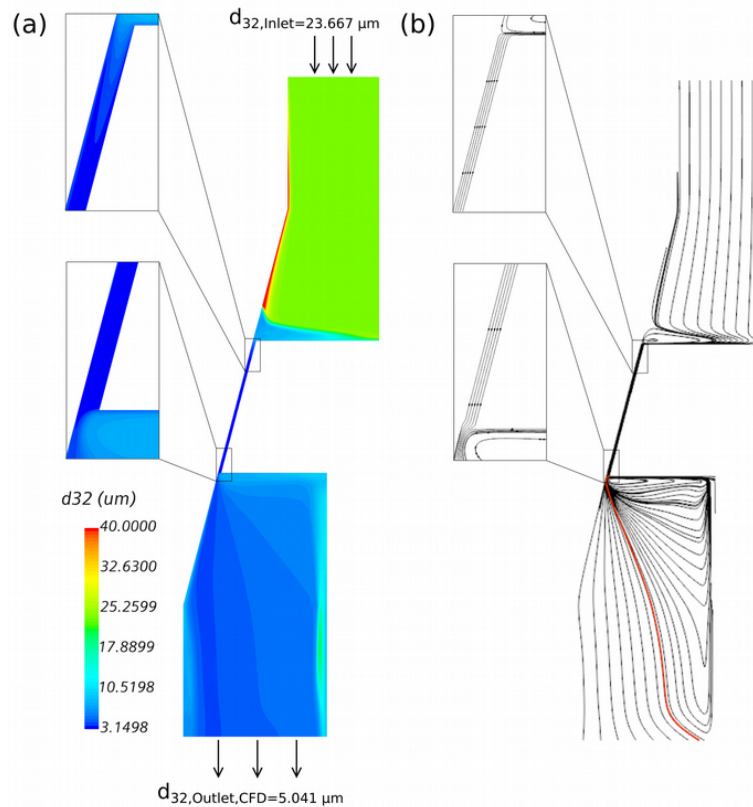
Fig. 17. (a) Contour of d_{32} and (b) streamlines for test case M3S1; $d_{32,\text{EXP}} = 4.647$ μm

3.2.4. Droplet dispersions for same emulsion and different operational conditions

Figures 18 and 19 show contours of d_{32} for the 70 wt% emulsion and operational conditions S2 and S3, respectively. Values of d_{32} at several locations of the two domains are reported in Table 6. In S2, the gap shear rate is significantly larger than that in S3 while the gap residence time is similar. Despite the gap shear rate in S3 being 6 times smaller than in S2, with viscosity as in Equation 10, the delivered d_{32} for S3 is only 1.4 times larger than in S2. In the inlet chamber, the effect of increasing flow rate is to suppress the recirculation region, similarly to the effect of increasing viscosity. The value of d_{32} at the entrance of the gap is much larger for S3; this is due to different shear rates in the boundary layer on the top of rotor as driven by the assigned rotational speed. Once the fluid has reached the gap, for S2 the minimum drop size is achieved closer to the gap entrance than for S3. In part this is because it was already smaller on entry but also because of the higher gap shear rate. At the gap exit, d_{32} is 1.6 μm for S2 and 5.1 μm for S3.

The values of d_{32} at the outlet are 5.6 μm and 7.7 μm, respectively so there is more coalescence in S2. A comparison between Figures 18b and 19b shows that S2 has a larger recirculation zone and a thinner layer of high shear near the underside of the rotor. This is consistent with the results of the previous section suggesting that a larger recirculation zone of modest shear rates allows coalescence to occur.
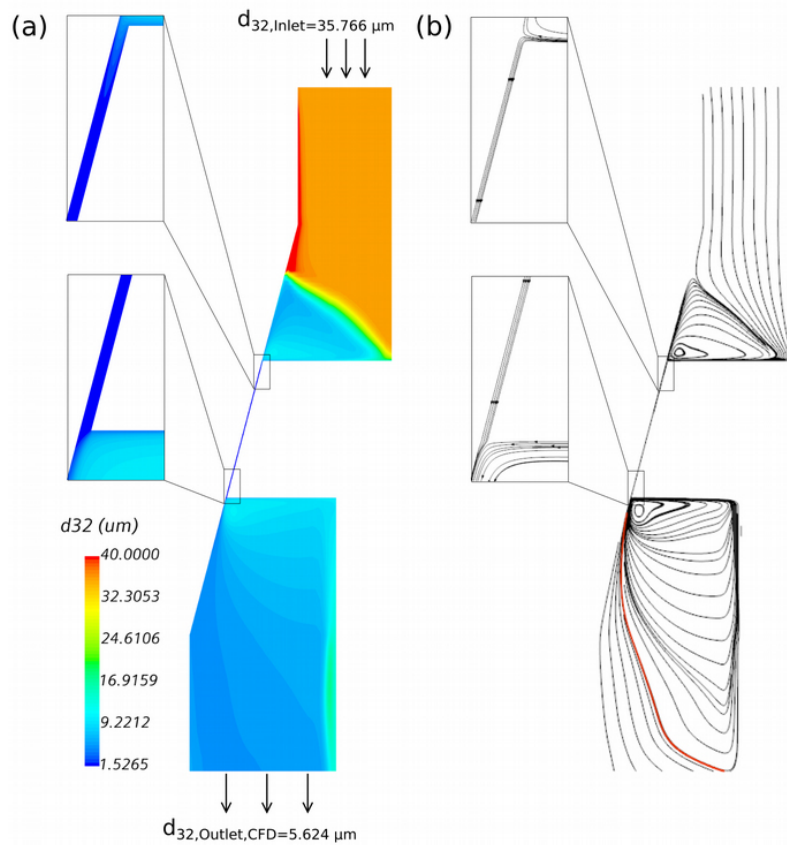
www.czasopisma.pan.pl   PAN   www.journals.pan.pl

G. Lupieri, I. Bagkeris, J.J.M. Janssen, A.J. Kowalski, Chem. Process Eng., 2021, 42 (4), 295–320

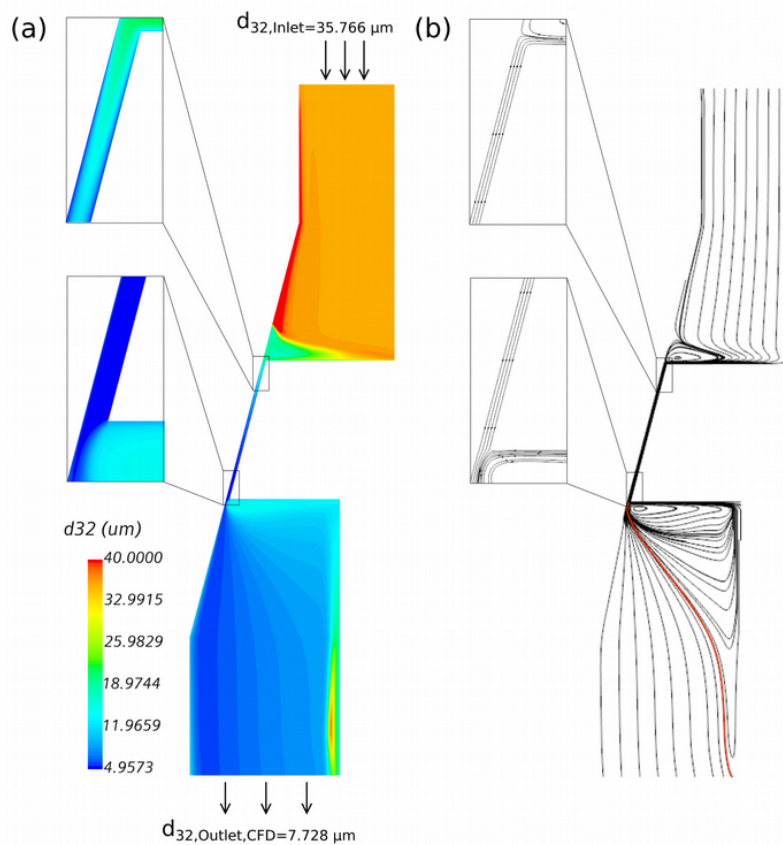Fig. 18. (a) Contour of d_{32} and (b) streamlines for test case M2S2; $d_{32,\text{EXP}} = 5.844$ μm

Fig. 19. (a) Contour of d_{32} and (b) streamlines for test case M2S3; $d_{32,\text{EXP}} = 7.713$ μm

3.3. Part III

The final geometry is CG3 in Figure 2c which includes two large grooved blades at its top. Their presence can affect the hydrodynamics in the inlet chamber: Figures 20a and 20b evidence the presence of a (permanent) rotating structure at the tip of the two rotor teeth that can extend downwards where there is space between the teeth.

Diversely, as sketched in Figure 8, in CG2 a similar feature was present at the flat top of the rotor and was identified as responsible for the recirculation of material in the inlet chamber. In the exit chamber the recirculation zones are still present but this time the exit is lateral.

(a)

(b)
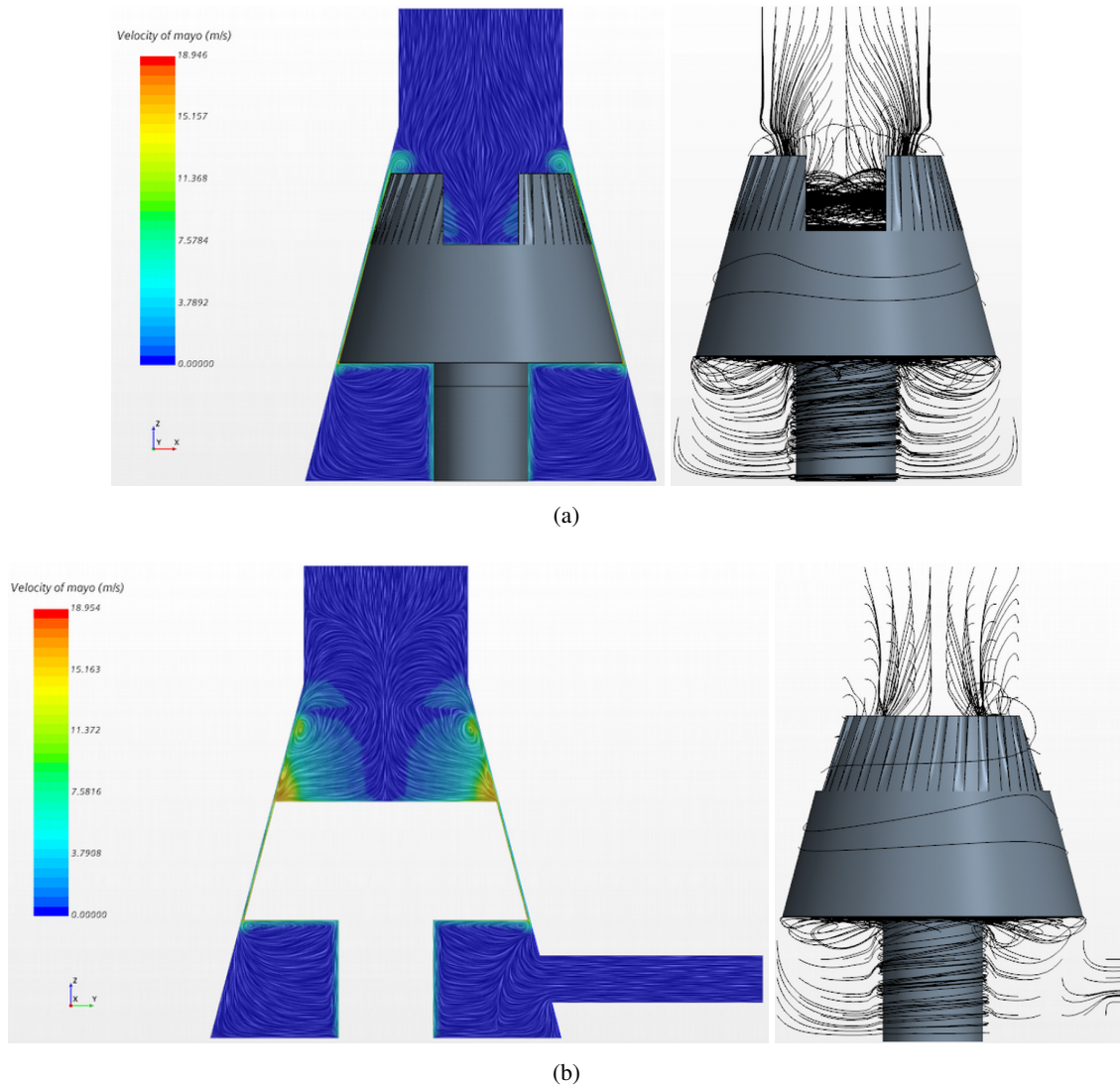
Fig. 20. Geometry 3: line integral convolution of the velocity field and streamlines
on *xz* plane (a) and on *yz* plane (b)

The velocity pattern is dominated in amplitude by the tangential component of the velocity while the axial component reveals a new mechanism that drives the fluid towards the gap. Figure 21 presents axial velocity component in two selected planes, at the top of the blade (Fig. 21a) and at half height (Fig. 21b). The fluid is pushed towards the gap mainly in two specific regions: at the leading edge of the blades (Fig. 21a) and down along the grooves (Fig. 21b), resulting in the complex recirculation pattern in the top chamber.

www.czasopisma.pan.pl PAN www.journals.pan.pl

G. Lupieri, I. Bagkeris, J.J.M. Janssen, A.J. Kowalski, Chem. Process Eng., 2021, 42 (4), 295–320
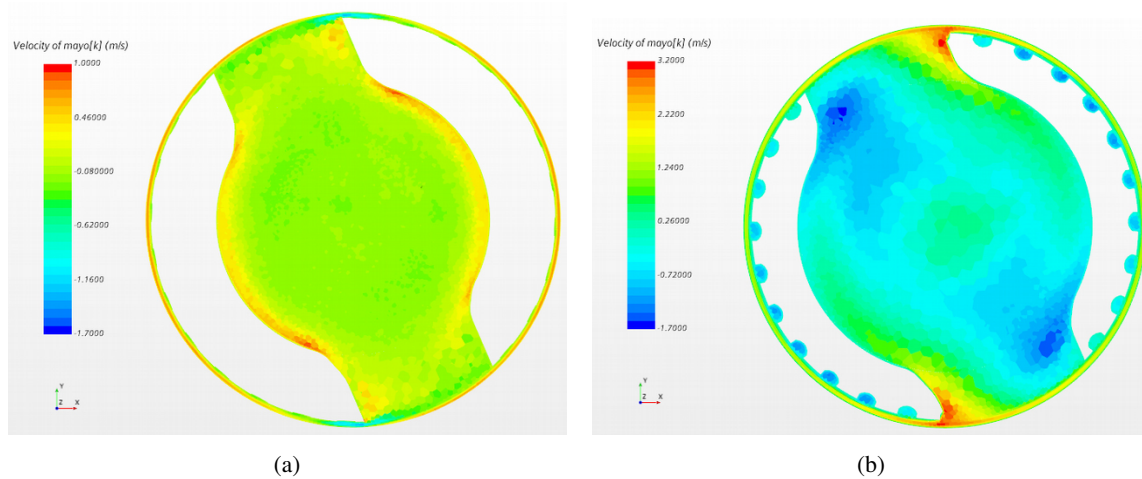
(a)   (b)

Fig. 21. Case M1S1, axial velocity at $z = 0.025$ m on (a) and $z = 0.035$ m on (b). Rotor is turning anti clockwise

Power consumption of Geometry 3 is reported for completeness of analysis in Table 7. In this case, the volume of fluid moved by rotor now includes the part processed by the blades and for this reason the final power consumption is 30–60% higher than in Geometry 2, Table 4. The presence of the blades and teeth increases the surface of rotor in contact with the fluid. Furthermore, the rotor teeth are subjected to a pressure difference between leading and trailing edges, similarly to the case of a blade subjected to an incident flow, suggesting that when pressure is included in the total power calculated on the rotor, it would be always higher than that for Geometry 2 in which pressure contributes were negligible.

Table 7. Geometry 3: power [W] calculated at the rotor from torque and pressure contributes

	S1	S2	S3	S4	S5
M1	184.5	505.7	57.7	184.1	123.5
M2	463.8	1475.5	140.0	463.4	336.8
M3	775.5	2290.2	240.3	755.2	524.3

The results of the population balance modelling are reported in Figure 22 and with reference to Table 5. As in the previous sections we could not get a unique set of tuning parameters and we see two groupings,
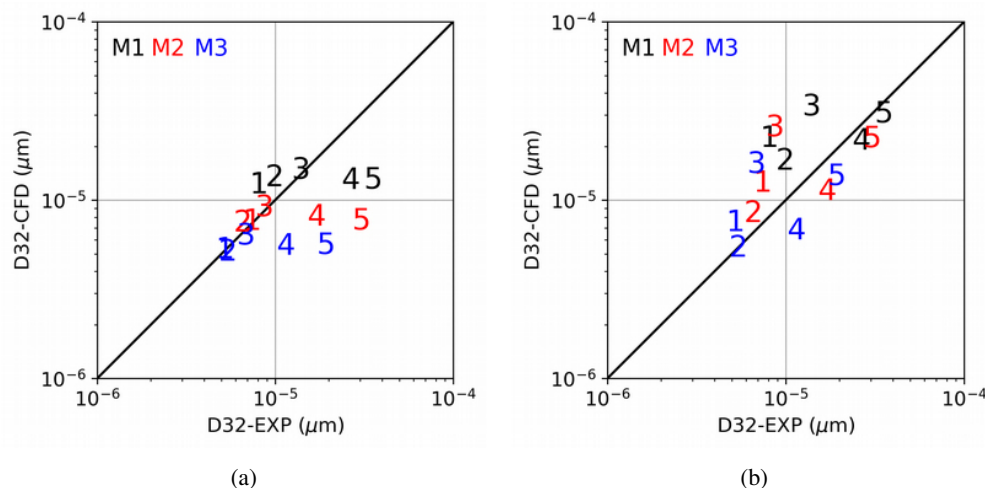

(a)   (b)

Fig. 22. Parity plot of d_{32} using two sets of model parameters shown in Table 5. Simulation labels refer to Table 2

cases S4 and S5 and then cases S1 to S3. Since the nominal shear (the one at the tip of the rotor base) is unchanged in Geometry 2 and Geometry 3, the small differences with the results in Figure 12 cannot suggest any modelling dependence if not strictly related to the differently assumed geometry.

4. CONCLUSION

The motivation for the work was to improve the prediction of emulsion drop size produced by a cone mill. It was intended to be preliminary to further studies on other high shear rotor stator devices. The assumption in most of previous works is that the gap, which has by far the highest shear rates, dominates the drop size reduction. However, for the cone mill two correlations were required, one for a similar gap shear rate and the other for similar residence times (Dubbelboer et al. (2016)). In this study we started from this simplified geometrical view and systematically reviewed the hydrodynamics and the impact on the population balance modelling as we added geometric features. The simplest geometry of a gap shows that the flow is not always simple shear with Taylor-Couette vortices forming at larger gaps and rotor speed though they are suppressed by increasing flow rate. Adding a top chamber produces a recirculation due to centrifugal drag forces which can produce significant drop size reduction before the fluid even enters the gap. Adding the large blades in the entry chamber disrupts this flow adding swirl but the shear between these blades and wall can cause drop break-up. Adding an exit chamber allows coalescence to occur and is related to the size of the recirculation zone. Despite this wealth of additional hydrodynamic features there was, unfortunately, little improvement to the quality of the prediction. This led to the view that the weak link is the PBM. More specifically it would be worth considering elongational and shear driven processes separately, for example K_4 was lower than expected suggesting a more effective breakup mechanism, such as elongational flows, on entry to the gap. This could account for the effect of the residence time grouping since this is related to flow rate and hence extensional flow into the gap. Moreover, the coalescence models are based on the draining of the interstitial fluid in dilute emulsions (Chesters, 1991) whereas in high phase volume emulsions the drops are almost touching and there is nowhere for the fluid to drain and so the physical basis for the constants is questionable. Consequently, there remain exciting scientific challenges in extending the foundational work in PBM of pioneers such as Prof. Bałdyga to products and process of industrial importance.

SYMBOLS

$b(d)$	breakage frequency
C	breakage time constant (non-dimensional)
Ca	capillary number
Ca_{crit}	critical capillary number
C_p	coalescence probability
C_r	coalescence collision rate per unit volume, $m^{-3}\,s^{-1}$
d_{32}	Sauter mean diameter of oil droplets, m
d_{eq}	equivalent diameter, m
d_{MAX}	maximum steady droplet size, m
K	consistency
K_1, K_2, K_3, K_4	tuning parameters
m	fit exponent
p	number of fragments
$P(d)$	particle size distribution

Re_a	axial Reynolds number
S	moment of S-γ method
S_{br}, S_{cl}	breakage and coalescence source terms
Ta	Taylor number
t_{br}	breakage time, s
t_{cl}	drain time, s

Greek symbols

ϕ_m	matrix phase fraction
ϕ_o	oil phase fraction
$\dot{\gamma}$	shear rate, s^{-1}
$\eta_{r,\infty}$	high shear plateau viscosity, Pa s
α	volume fraction
η_a	aqueous phase viscosity, Pa s
η_{em}	apparent emulsion viscosity, Pa s
η_R	relative viscosity
ρ_m	density of continuous phase, kg m^{-3}
ρ_o	density of oil, kg/m^3

Subscripts

$\gamma = 0, 2, 3$	number of moments in S-γ method

ACKNOWLEDGEMENTS

REFERENCES

Alopaeus V., Koskinen J., Keskinen K.I., 1999. Simulation of the population balances for liquid-liquid systems in a nonideal stirred tank. Part 1 Description and qualitative validation of the model. *Chem. Eng. Sci.*, 54, 5887–5899. DOI: 10.1016/S0009-2509(99)00170-0.

Bałdyga J., Jasińska M., Kotowicz M., Tyl G., Bouaifi M., 2018. Population Balance Equations: fundamentals, challenges, application, limitations and perspectives. *Conference: 23rd International Congress of Chemical and Process Engineering. CHISA 2018*, Prague.

Bałdyga J., Jasińska M., Kowalski A.J., 2016. Effect of rheology of dense emulsions on the flow structure in agitated systems. *Chem. Eng. Res. Des.*, 108, 3–12. DOI: 10.1016/j.cherd.2015.11.026.

Bałdyga J., Orciuch W., Makowski Ł., Malski-Brodzicki M., Malik K., 2007. Break up of nano-particle cluster in high-shear devices. *Chem. Eng. Process. Process Intensif.*, 46, 851–861. DOI: 10.1016/j.cep.2007.05.016.

Bałdyga J., Podgórska W., 1998. Drop break-up in intermittent turbulence: Maximum stable and transient sizes of drops. *Can. J. Chem. Eng.*, 76, 456–470. DOI: 10.1002/cjce.5450760316.

Bentley B.J., Leal L.G., 1986. An experimental investigation of drop deformation and breakup in steady, two-dimensional linear flows. *J. Fluid Mech.*, 167, 241–283. DOI: 10.1017/S0022112086002811.

Buffo A., De Bona J., Vanni M., Marchisio D.L., 2016. Simplified volume-averaged models for liquid-liquid dispersions: Correct derivation and comparison with other approaches. *Chem. Eng. Sci.*, 153, 382–393. DOI: 10.1016/j.ces.2016.07.032.

Buffo A., Ferrari M., Boccardo G. and Marchisio D.L., 2019. Numerical simulation of a high-shear cone mill mixer for food emulsions production. *ECCE12, 12th European Congress of Chemical Engineering*. Florence, Italy, 15-19 September 2019. *Book of abstracts*, 650–651. DOI: 10.3303/BOA1901.

Chesters A.K., 1991. Modelling of coalescence processes in fluid-liquid dispersions. A review of current understanding. *Chem. Eng. Res. Des.*, 69(4), 259–270.

de Bruijn R.A., 1989. *Deformation and breakup of drops in simple shear flow*. PhD Thesis, Technische Universiteit Eindhoven. DOI: 10.6100/IR318702.

Dubbelboer A., 2016. *Towards optimization of emulsified consumer products: modelling and optimization of sensory and physicochemical aspects*. PhD Thesis, Technical University of Eindhoven.

Dubbelboer A., Janssen J., Hoogland H., Mudaliar A., Maindarkar S., Zondervan E., Meuldijk J., 2014. Population balances combined with Computational Fluid Dynamics: A modeling approach for dispersive mixing in a high pressure homogenizer. *Chem. Eng. Sci.*, 117, 376–388. DOI: 10.1016/j.ces.2014.06.047.

Dubbelboer A., Janssen J.J.M., Hoogland H., Zondervan E., Meuldijk J., 2016. Pilot-scale production process for high internal phase emulsions: Experimentation and modeling. *Chem. Eng. Sci.*, 148, 32–43. DOI: 10.1016/j.ces.2016.03.014.

Grace H.P., 1982. Dispersion phenomena in high viscosity immiscible fluid systems and application of static mixers as dispersion devices in such systems. *Chem. Eng. Commun.*, 14, 225–277. DOI: 10.1080/00986448208911047.

Håkansson A, Trägårdh C., Bergenståhl B., 2009. Studying the effects of adsorption, recoalescence and fragmentation in a high-pressure homogenizer using a dynamic simulation model. *Food Hydrocolloids*, 23, 1177–1183. DOI: 10.1016/j.foodhyd.2008.10.003.

IKA, 2020. Commercial brochure. Available at: https://www.ika.com/.

Jansen K.M.B., Agterof W.G.M., Mellema J., 2001. Droplet breakup in concentrated emulsions. *J. Rheol.*, 45, 227–236. DOI: 10.1122/1.1333001.

Janssen J.J.M., Hoogland H., 2014. Modelling strategies for emulsification in industrial practice. *Can. J. Chem. Eng.* 92, 198–202. DOI: 10.1002/cjce.21942.

Janssen J.J.M., Mayer R., 2016. Computational Fluid Dynamics (CFD)-based droplet size estimates in emulsification equipment. *Processes*, 4, 50. DOI: 10.3390/pr4040050.

Jasińska M., Bałdyga J., Hall S., Pacek A.W., 2014. Dispersion of oil droplets in rotor-stator mixers: Experimental investigations and modelling. *Chem. Eng. Process. Process Intensif.*, 84, 45–53. DOI: 10.1016/j.cep.2014.02.008.

Li X., Zang Jj., Xu Lx., 2014. A numerical investigation of the flow between rotating conical cylinders of two different configurations. *J. Hydrodyn.*, 26, 431–435. DOI: 10.1016/S1001-60581460049-4.

Lo S., Zhang D., 2009. Modelling of break-up and coalescence in bubbly two-phase flows. *J. Comput. Multiphase Flows*, 1, 23–38. DOI: 10.1260/175748209787387106.

Lupetow R.M, Docter A., Min K., 1992. Stability of axial flow in an annulus with a rotating inner cylinder. *Phys. Fluids A*, 4, 2446. DOI: 10.1063/1.858485.

Lupieri G., Kowalski A.J., Janssen J.J.M., 2019. Numerical modelling of emulsion preparation through CFD. *ECCE12, 12th European Congress of Chemical Engineering*. Florence, Italy, 15-19 September 2019. *Book of abstracts*, 556–557. DOI: 10.3303/BOA1901.

Maindarkar S., Dubbelboer A., Meuldijk J., Hoogland H., Henson M., 2014. Prediction of emulsion drop size distributions in colloid mills. *Chem. Eng. Sci.*, 118, 114–125. DOI: 10.1016/j.ces.2014.07.032.

Noui-Mehidi M.N., Ohmura N., Kataoka K., 2002. Mechanism of mode selection for Taylor vortex flow between coaxial conical rotating cylinders. *J. Fluids Struct.*, 16, 247–262. DOI: 10.1006/jfls.2001.0417.

Noui-Mehidi M.N., Ohmura N., Kataoka K., 2005. Dynamics of the helical flow between rotating conical cylinders. *J. Fluids Struct.*, 20, 331–344. DOI: 10.1016/j.jfluidstructs.2004.12.001.

Park H.M., 2018. Comparison of the pseudo-single-phase continuum model and the homogeneous single-phase model of nanofluids. *Int. J. Heat Mass Transfer*, 120, 106–116. DOI: 10.1016/j.ijheatmasstransfer.2017.12.027.

Rapley S., Eastwick C., Simmons K., 2008. Computational investigation of torque on coaxial rotating cones. *J. Fluid Eng.*, 130, 061102. DOI: 10.1115/1.2903518.

Wieringa J.A., van Dieren F., Janssen J.J.M., Agterof W.G.M., 1996. Droplet breakup mechanism during emulsification in colloid mills at high dispersed phase volume fraction. *Trans IChemE A*, 74, 554–562.